Chemical Engineering Journal Advances 16 (2023) 100565

Contents lists available at ScienceDirect

Chemical Engineering Journal Advances

journal homepage: www.sciencedirect.com/journal/chemical-engineering-journal-advances

Phosphate burial in aquatic sediments: Rates and mechanisms of vivianite formation from mackinawite

Mingkai Ma [a,*], Peter Overvest [a], Arjan Hijlkema [a], Stefan Mangold [d], Catherine McCammon [c], Andreas Voegelin [b], Thilo Behrends [a]

[a] Department of Earth Sciences, Faculty of Geosciences, Utrecht University, Princetonlaan 8, Utrecht 3584 CB, the Netherlands
[b] Eawag, Swiss Federal Institute of Aquatic Science and Technology, Überlandstrasse 133, Dübendorf CH-8600, Switzerland
[c] Bayerisches Geoinstitut, University of Bayreuth, Bayreuth 95440, Germany
[d] Institute for Photon Science and Synchrotron Radiation, Karlsruhe Institute of Technology, Hermann-von-Helmholtz-Platz 1, Eggenstein-Leopoldshafen, Karlsruhe 76344, Germany

ARTICLE INFO

Original content: FeS2viv_Ma_etal_2023

Keywords:
Early diagenesis
Authigenic vivianite formation
Mackinawite
Mössbauer spectroscopy
X-ray absorption spectroscopy

ABSTRACT

Excess phosphorus abundance often drives eutrophication and affects surface water quality. Formation of vivianite ($Fe_3(PO_4)_2 \bullet 8H_2O$) in aquatic sediments acts as a significant sink for phosphate (P), crucial for resorting surface waters. Authigenic vivianite formation, however, can be limited by other ferrous iron containing phases, in particular iron sulfides. Although thermodynamically feasible under suitable conditions, the formation of vivianite from mackinawite has been widely disregarded for authigenic phosphate mineral formation. Here we investigated the formation of vivianite from mackinawite (FeS) in batch experiments in which dissolved sulfide was continuously removed, at P levels between 0 – 5 mM in a pH of 6 to 8. Solid characterizations by electron microscopy, X-ray diffraction as well as Mössbauer and X-ray absorption spectroscopy demonstrates that vivianite was formed at all pH values in P amended experiments. The temporal evolution of dissolved Fe(II) concentrations indicates that the transformation proceeds via the release of the dissolved Fe(II) by FeS dissolution and subsequent vivianite precipitation, over time scales of days. The kinetics of the transformation are controlled by the dissolution rates of FeS. Aging and transformation of FeS, however, compete with vivianite formation. Aging is more pronounced at higher pH but is inhibited by P adsorption. Hence, the effect of pH and P concentration on aging is the main reason for the influence on these parameters on the rates and extent of vivianite formation. Our findings demonstrate that FeS can be an effective iron source for vivianite formation in aquatic sediments when sulfide concentrations decrease due to, for example, changes in external forcing or microbial sulfide oxidation. Formation of vivianite from FeS as an Fe source can also open new perspectives in P recovery in water treatment, for example when Fe is added to digesters to bind H_2S.

1. Introduction

Phosphorus is an essential element to organisms and, consequently, a key regulating factor for primary production in aquatic ecosystems. However, excessive phosphorus often aggravates eutrophication in aquatic systems. Besides reducing the anthropogenic input of phosphorus to waterbodies, increasing of phosphorus burial in the sediments could also be a mitigation strategy to reduce phosphorus levels [1]. During early diagenesis, phosphorus can be mobilized from organic and inorganic solids by, e.g. reduction of iron (hydr)oxides with sorbed phosphorus and decomposition of organic matters, in the form of dissolved phosphate (PO_4^{3-}, hereafter P). The mobilized P can be transferred to the overlying water and thus exacerbated P excess. However, the liberated P can also be re-immobilized by the formation of authigenic P-containing minerals, presenting a pathway for long term P retention in sediments. Relevant authigenic P-bearing minerals include calcium phosphates, such as apatite, and phosphates forming with ferrous (Fe(II)) and ferric (Fe(III)) iron. Under reducing conditions, vivianite ($Fe_3(PO_4)_2 \bullet 8H_2O$) is the most stable mineral among the various iron orthophosphates [2]. Authigenic vivianite has been detected in many freshwater environments ([3] and references therein) and has been proposed already early on to be a result of the reduction of Fe

* Corresponding author.
E-mail address: m.ma@uu.nl (M. Ma).

https://doi.org/10.1016/j.ceja.2023.100565

Available online 12 October 2023

(III) phosphates or Fe(III) hydroxides with adsorbed P (for example [4]). In the context of eutrophication abatement, the significance of vivianite as a possible sedimentary sink for P has been acknowledged (for example [2]) and has been integrated in mitigation strategies of eutrophic lakes based on iron addition [5,6]. Reports on vivianite authigenesis in marine sediments are scarce but it has been shown that vivianite can also present a major sink for P in marine systems [7–9]. In marine systems, the role of vivianite in P sequestration has been widely ignored due to the high sulfate concentrations in sea water. Due to the high abundance of sulfate, sulfide (hereafter S(-II)) production upon sulfate reduction typically exceeds the extent of Fe(II) production and, consequently, S (-II) competes with P for Fe^{2+} to form iron sulfides, such as mackinawite (FeS), pyrite (FeS_2) and pyrrhotite ($Fe_{1-x}S$). In pyritic environments, pyrite is often the only stable iron phase [10]. Despite the antagonism between the authigenic formation of vivianite and iron sulfides, the concurrence of both iron phases has been commonly reported [11–13]. The competition between authigenesis of different Fe minerals is essentially governed by thermodynamics and kinetics [14]. Co-existence of Fe-S (e.g. FeS), Fe-CO_3 (e.g. siderite) or Fe-P (e.g. vivianite) can be a consequence of preferential precipitation of one phase until the corresponding anion becomes exhausted and the next phase takes over, or can be a consequence of small-scale heterogeneity in the sediments. Simultaneous precipitation is also possible when the growth of the most stable mineral is kinetically retarded and precipitation of metastable phases is enabled. Finally, co-existence can also be the consequence of non-steady state conditions during early diagenesis. Particularly, the composition of pore water surrounding Fe minerals can change over time. This can be the case because of the burial and convective movement of minerals into sediment layers with different pore water composition, or changes in pore water composition driven by variable external forcing (e.g. changes in sulfate concentration or oxygen concentration in the overlying water, organic carbon burial rates etc.), or due to emerging or elusive biological activity (e.g. bioturbation or cable bacteria colonization). For example, cable bacteria use their filaments for long-distance electron transfer [15] and are able to oxidize S(-II) in deeper sediment layers by using oxygen in the upper part of the sediment as an electron acceptor. In combination with the acidity production due to S(-II) oxidation, FeS dissolution can be greatly enhanced by the activity of filamentous cable bacteria [16–18]. As a consequence, Fe^{2+} is released into the pore water and the formation of vivianite could be promoted. This is one of the possible scenarios that formation of vivianite from mackinawite could be enabled in aquatic sediments. However, this pathway for vivianite formation has not received attention so far. To our knowledge, experimental studies on the transformation from FeS to vivianite are lacking and the mechanism as well as the kinetics of this transformation are unknown.

The transformation from FeS to vivianite is expected to be a dissolution-precipitation process instead of solid-solid phase transition, due to higher activation energy required for the latter mechanism [19]. Hence, the process can be schematically represented by a sequence of the following two reversible reactions:

$$FeS\ (s) + H^+ \rightleftharpoons Fe^{2+} + HS^- \quad \text{(Step 1)}$$

$$3Fe^{2+} + 2PO_4^{3-} + 8H_2O \rightleftharpoons Fe_3(PO_4)_2{\cdot}8H_2O(s) \quad \text{(Step 2)}$$

This implies, that the overall rate could be limited by either of the two steps. Pankow and Morgan [20] developed a rate law for the dissolution of FeS yielding rates around 2 10^{-5} mol m^{-2} min^{-1} at circumneutral pH and 25 C°. This value represents rates far from equilibrium and the dissolution is expected to proceed slower close to equilibrium when the reverse reaction becomes relevant. Also the growth kinetics of vivianite depend on the distance from equilibrium and rates between 2 10^{-9} and 2 10^{-13} m s^{-1} have been reported at 35 C° [21], corresponding to Fe normalized growth rates between around 2 10^{-3} and 2 10^{-7} mol Fe m^{-2} min^{-1} for saturation indices between approximately 4.3 to 2.2, respectively. For comparison, the dependency on saturation indices has also been reported for fluorapatite growth in seawater where values decrease from 2.5 10^{-7} to 1.3 10^{-8} mol Ca m^{-2} min^{-1} for saturation indices decreasing from 1.7 to 1.4 [22], respectively. When ignoring differences in interfacial area of vivianite and FeS, these data lead to the hypothesis that, if thermodynamically possible and at circumneutral pH, vivianite growth will be limiting the formation of vivianite from mackinawite until the solution is moderately supersaturated with respect to vivianite and reaches values for the saturation index (SI) above 2. The hypothesis corresponds with the findings of Liu et al. [23] from reactor experiments, who reported that efficient vivianite crystallization required SI values above 4.0. These considerations are based on reported rates of vivianite growth and do not consider vivianite nucleation. It is possible that heterogenous nucleation occurs on the surface of FeS particles, which can potentially lead to FeS overgrowth and other feed-back mechanisms. In any case, the reported rates also suggest, when assuming specific surface areas in the range of tenths or hundreds m^2 g^{-1} that a considerable fraction of FeS can transform into vivianite within hours to days.

In this study, we aim to experimentally verify that transformation of vivianite from FeS is possible and can occur within hours to days. In order to test the hypotheses about the formation mechanism and kinetics, we performed experiments in a pH range between 6.0 and 8.0 and varied the phosphate concentrations. By this, the thermodynamic driving force of the transformation was varied, which is expected to be reflected in the rates of the reaction.

2. Material and methods

2.1. Apparatus and chemicals

Mineral synthesis, solution preparation, setting up experiments and all manipulations with sampled solids were performed in a glove box under N_2 atmosphere (> 99.99%) to minimize oxidation artefacts. Deionized water (DI water, < 18.2 MΩ) was used for all solutions. For removing dissolved oxygen, DI water was purged with N_2 gas for at least one hour prior to use. This method leaves dissolved oxygen in the water at concentrations around 6 uM [24], which were conceived neglectable compared to the applied FeS concentrations. All chemicals were of at least analytical grade and used without any further purification.

2.2. FeS synthesis

The FeS synthesis was conducted following Wolthers et al. [25] by producing a precipitate frequently referred to as disordered or amorphous FeS. Briefly, 100 mL of 0.6 M Na_2S solution (sodium sulfide nonahydrate, Sigma-Aldrich, BioUltra) was mixed with 100 mL of a solution of 0.6 M Mohr's salt (Ammonium Fe(II) sulfate hexahydrate, Sigma-Aldrich, ACS reagent). Blackish precipitates formed instantaneously and were filtered by using a paper filter (⌀ 185 mm, Schleicher & Schuell 595). The precipitates were first collected in a glass bottle sealed with rubber lids to prevent oxidation, and only opened before freeze-drying. After freeze-drying, the bottle was sealed again and wrapped with aluminum foil to avoid photochemical reactions. The solids were kept at −20 °C to retard any solid phase transformations.

2.3. Experimental setup

Batch experiments were carried out in duplicates at pH 6.0, 7.0 and 8.0 which was maintained during the experiment using 10 mM buffer solutions: MES for pH 6.0 (Calbiochem, $pK_a = 6.10$ at $T = 25$ °C), HEPES buffer for pH 7.0 (Sigma-Aldrich, $pK_a = 7.48$ at $T = 25$ °C) and PIPPS buffer for pH 8.0 (Calbiochem, $pK_a = 7.96$ at $T = 25$ °C). The pH was adjusted by using HCl or NaOH, respectively, and checked at the end of the experiments. No significant changes in pH were observed. 0.01 M NaCl (EMSURE) was added to the buffer solution as a background

electrolyte. Phosphate levels of 0.0, 1.0, 2.5, and 5.0 mM were established by the addition of 0.333 M NaH_2PO_4 (Calbiochem) or 0.5 mM Na_2HPO_4 (Sigma-Aldrich) stock solutions. Depending on the target pH value: 100% of NaH_2PO_4 was added for experiments at pH 6, 50% of NaH_2PO_4 and 50% of Na_2HPO_4 at pH 7, and 100% of Na_2HPO_4 was added to pH 8 experiments. This was done to reduce the influence on pH upon adding phosphate solution caused by the transformation among different phosphate species.

The experiments were prepared in serum glass bottles (125 mL). First, 100 mL of background electrolyte containing the buffer solutions was added to the bottles, then ~10 mg of freeze-dried FeS was weighed and subsequently added to the solutions. This resulted in a starting FeS concentration of ~1.2 mM. Subsequently, P was added correspondently to the target P concentrations (0.0, 1.0, 2.5 and 5.0 mM). After the addition of chemicals, the bottles were closed with a rubber stopper, which was secured with an aluminum screw cap. After preparation, the bottles were transferred out of the glove box and kept in a lying position on a horizontal shaker at 120 rpm at 21 ± 1 °C during the whole experiment. Before installation on the shaker, all suspensions were sonicated (Branson 3800) for 5 min to resuspend the FeS particles. Additionally, the serum bottles were wrapped in aluminum foil to prevent light-induced redox reactions.

In preliminary tests, we have established that the rubber stoppers are an effective sink for dissolved S(-II), possibly via binding to the polysulfide crosslinks or remaining elemental sulfur in the rubber. Hence, the experiment mimics an environmental setting in which FeS dissolution is driven by the removal or consumption of dissolved S(-II), for example, by anaerobic S(-II) oxidation [26]. Correspondingly, the anticipated equilibrium vivianite formation has been calculated for two extreme conditions: closed system and fixed, negligible H_2S pressure and is presented in Fig. S1.

2.4. Sampling and chemical analysis

Aliquots were taken repeatedly during the experiments. Before sampling, the bottles were put into an ultrasonic bath for 5 min in order to homogenize the suspension. 2 mL of the suspension was taken by using a syringe with a needle. Prior to each sampling, 2 mL N_2 gas was injected from an N_2-filled syringe to avoid a negative pressure in the bottle that could have caused ingress of atmospheric O_2. The suspension was quickly filtered through a nylon filter (⌀ 13 mm, 0.2 μm pore size, Mdi) to separate suspended solids from the solution. The filtrate, considered to contain only dissolved species, was separated into two aliquots: One aliquot (0.5 mL) was added to 10 mL of 0.2% Zn-acetate to retain and preserve S(-II). The other aliquot (1 mL) was added to 0.2 mL 6 M HCl to remove S(-II) by converting it into H_2S and to prevent Fe(II) oxidation, hence preserving dissolved Fe and P. Afterwards, the filter was flushed with 1 ml of deoxygenized DI water and then slowly extracted with 1 mL of 6 M HCl in order to dissolve the retained solids on the filter for determining solid-bound Fe and P. Sulfide concentrations were regularly determined at the beginning of the experiment but only occasionally in a later stage, as the concentrations were constantly below the detection limit by the methylene blue method (<1 μM). In addition, dedicated samples were collected after 37 days reaction time to determine total Fe(II) and Fe(III) concentrations. This was done to ascertain that Fe(II) remained in reduced state throughout the experiment. For this, a sample of 2 mL was collected inside the glove box and added directly to 1 mL of 6 M HCl without a filtration step.

Concentrations of S(-II), Fe(II), Fe(III) and PO_4^{3-} in the filtered solutions were determined photometrically: S(-II) was measured using the diamine reagent following the method of Fonselius et al. [27]. Fe(II) and Fe(III) concentrations were measured according to the revised Ferrozine method [28], with extra buffer added to neutralize 6 M HCl. The ascorbic acid method was used to determine PO_4^{3-} concentrations following the protocol of Hansen and Koroleff [29].

2.5. Characterization of solids

Solids were retrieved after 37 days of incubation by filtration through cellulose acetate filters (0.2 μm, OE66 Whatman), using syringes and a membrane holder (13 mm diameter, Whatman) inside the glovebox. Prior to retrieving the solids, the mineral suspensions were dispersed in an ultrasonic bath. The collected solids were rinsed with O_2-free DI water to remove salts and dried under an N_2 gas flow inside the glove box. The retrieved solids, together with the filter, were collected in a petri dish. The petri dish was then sealed with parafilm, put into a bag made out of triplex foil containing an Al layer, closed and kept inside the glove box until further analysis.

2.5.1. X-ray diffraction

The X-ray diffraction (XRD) measurements were carried out using an air-tight sample holder (Airtight specimen holder with knife edge, Bruker). The retrieved solids on the membrane were fixed on the holder with double-sided tape, and because of the limited sample mass, the diffractograms contained a broad background peak at ~ 27° originating from the tape or filter membrane. The XRD analysis was performed on a Bruker AXS D8 ADVANCE X-ray diffractometer with Copper K-α radiation (40 kV, 40 mA) over the range 2θ from 8 – 50°, the integration time of 2 s and step size of 0.02°. The software Diffrac.DEV 3.0 (Bruker) was used for analyzing the XRD data.

2.5.2. Transmission electron microscope

Dry solids were dispersed in 0.5 mL ethanol (biological molecular grade, Sigma-Aldrich,) in 2 mL tubes (Eppendorf) inside the glove box. To homogenize the suspension, the tube was firstly sealed, removed from the glove box and then put into an ultrasonic bath for 10 min. After ultra-sonification, the tubes were transferred back into the glove box and TEM samples were prepared by adding 20 μl of the mineral suspension to a holey carbon grid (200 mesh, Agar Scientific) and left until dry. Each sample was then put into a storage box (rotary with 6 positions, Agar Scientific) and then sealed with parafilm separately. The storage box was then put into an PP sealing bag, and then heat-sealed with N_2 gas to maintain anoxic conditions during sample transportation.

For the TEM measurements, samples were loaded as quickly as possible into the TEM holder. Transmission electron microscope (TEM) measurements were performed on a FEI Talos F200X microscope, equipped with four energy-dispersive X-ray detectors (Super-X EDX) at the electronic microscopy Electron Microscopy Square, Utrecht University. The images were measured with 200 kV acceleration voltage. For the TEM image processing, Velox 3.6.0 (Thermo Scientific) was used for labeling and marking areas, and ImageJ was used for quantifying dimensions in the micrographs without any further image manipulation. Fityk 1.3.1 was used to fit the EDS spectra, and the relative content of S, Fe and P were calculated by the obtained peak areas and later normalized.

2.5.3. X-ray absorption spectroscopy

For preparing samples for X-ray absorption spectroscopy (XAS) measurements at the Fe K-edge, an amount of the dried solids collected after 37 days corresponding to ~1 mg of Fe was mixed with 100 mg of cellulose (microcrystalline, <20 μm particle size, Sigma-Aldrich). For this, about a quarter of the freeze-dried cellulose filter membrane covered by the solids was ground in an agate mortar together with the cellulose. The mixtures were then pressed into 7-mm diameter pellets using a hand pellet press (PIKE technologies). After preparation, the pellets were placed on pellet holders (9 samples per holder) that was covered on both sides with Kapton® tape. The sample holders were placed in N_2-filled bags made from triplex aluminum foil which were sealed for shipment to the synchrotron.

The XAS measurements were performed at the XAS beamline at the KIT Light Source (Karlsruhe Institute of Technology, Germany). Inside a glove box, the sample holders containing the Kapton®-sealed pellets were

removed from the N_2-filled bags and mounted inside a vacuum chamber, preventing any air contact. The measurements were performed at room temperature in transmission mode, using ionization chambers for the analysis of the incoming and transmitted X-ray intensity. A double-crystal monochromator was used for energy selection, and was calibrated by setting the first maximum of the first derivative of the spectrum of a metallic Fe foil to 7112 eV On each sample, between 3 and 14 scans were collected and merged. Together with the samples, reference spectra of synthetic FeS, vivianite and lepidocrocite were collected. Reference spectra of an amorphous basic Fe(III)-phosphate [30] and of a natural pyrite specimen were available from earlier measurements. The X-ray absorption near-edge structure (XANES) and extended X-ray absorption fine edge structure (EXAFS) spectra were extracted and evaluated using the software code Athena [31]. For the extraction of the normalized XANES spectra, E_0 was set to 7128.5 eV, a linear function was fit to the pre-edge region (−100 to -30 eV before E_0) for background removal, and a cubic function to the post-edge region (50-400 eV above E_0) for normalization. For the extraction of the EXAFS spectra, the Autobk algorithm was used (R_{bkg} = 0.85; *k*-weight = 3; spline *k*-range 0–11.8 $Å^{-1}$). The XANES spectra were analyzed by linear combination fitting (LCF) over the energy-range from - 40 eV to +100 eV around E_0, and the k^3-weighted EXAFS spectra over the *k*-range 2–10.5 $Å^{-1}$. Based on preliminary tests (principal component analysis, target testing, and LCF analyses), five reference spectra (mackinawite, vivianite, lepidocrocite, amorphous basic Fe(III)-phosphate and pyrite) were selected to fit the XANES and EXAFS spectra. For fitting, the fractions of the individual components were constrained to values between 0 and 1, whereas the sum of the fractions was not constrained.

2.5.4. Mössbauer spectroscopy

Additional experiments dedicated to produce samples for Mössbauer spectroscopy were conducted at pH 6.0, 7.0 and 8.0 with 5 mM P materials that were enriched in ^{57}Fe (20% of total Fe) to enhance the signal. For this, $^{57}Fe_2O_3$ (Sigma-Aldrich) was dissolved in aqua regia (3: 1 HNO_3: HCl) and subsequently reduced with hydroxylamine (Sigma-Aldrich); the $^{57}Fe(II)$ concentration was constantly monitored during the process to ensure complete reduction. After $^{57}Fe(III)$ was fully reduced by hydroxylamine, the $^{57}Fe(II)$ solution was then neutralized by adding 1 M NaOH from pH 0.06 to about 3.0 under anoxic conditions. To synthesize 20% ^{57}Fe - enriched FeS, the method mentioned above from Wolthers et al. [25] was followed with some slight modification. Here the Fe(II) solution was composed of the $^{57}Fe(II)$ solution plus Fe(II) chloride tetrahydrate ($FeCl_2 \cdot 4H_2O$, Acros Organics) to obtain a 20%-labelled ^{57}Fe solution. Subsequently, Na_2S was added and a black suspension formed immediately. The pH was checked regularly after each chemical addition, and kept at ~3 by adjusting with HCl or NaOH. After synthesis of ^{57}FeS, the experiments were set up directly by adding ^{57}FeS, following the description above with 5 mM P loading.

The solids were retrieved inside the glove box after 29 d reaction time and prepared for Mössbauer analysis following methods described by Wan et al. [32]. For this, 20 mL of the suspension for each treatment was filtered with a cellulose membrane filter (Whatman, 13 ∅ mm, 0.45 μm) until the filter was clogged. Two filters were used for each sample. Then the retrieved solids were wrapped in Kapton tapes (sandwich-like) and the excess Kapton tape was cut to fit into the sample holder of the cryostat cold finger. Samples were transported in a sealed bottle and either stored in a freezer at −26 °C or loaded directly into the cryostat at 80 K. For the Mössbauer measurement, a constant acceleration Mössbauer spectrometer was used in transmission mode with a nominal 1.85 GBq ^{57}Co source in 6 μm Rh matrix. The velocity scale was calibrated relative to α-Fe. Samples were measured at 80 K in a Janis continuous flow cryostat cooled with liquid nitrogen. The whole measurement time for each spectrum ranged between 8 and 16 h. Samples were stored in the freezer in between measurements. To check for alteration during freezer storage, we compared the spectrum of pH 6 measured immediately after transport with one collected after 2 days of storage at −26 °C and saw no evidence for changes. For data fitting, we used MossA [33] for the pH 6 spectrum and Recoil [34] for the pH 7 and pH 8 spectra.

2.6. Thermodynamic calculations

Visual MINTEQ 3.1 was used for chemical equilibrium calculations [35] using the corresponding data base thermo.vdp. Values for the SI of vivianite were calculated based on the measured Fe(II) and P concentrations and the adjusted pH:

$$SI = \log\left(\frac{IAP}{K_{sp}}\right)$$

where K_{sp} is the solubility product and IAP denotes the ion activity product of vivianite. For the solubility product of vivianite $K_{sp\ vivianite} = 10^{-35.80}$ (294 K, [36]) was used and IAP was calculated based on:

$$IAP = \left\{Fe^{2+}\right\}^3 \cdot \left\{PO_4^{3-}\right\}^2$$

With activities calculated based on measured concentrations and activity coefficients obtained based on the Davies equation.

3. Results

3.1. Time evolution of the chemical composition of the suspension

Initial concentrations of dissolved Fe(II) ($Fe(II)_{aq}$), measured 4 h after starting the experiments, ranged between 18 and 250 μM in the control treatments without P loading, and decreased with increasing pH (Fig. 1a, 1b and 1c). The time evolution of FeS dissolution, reflected in $Fe(II)_{aq}$ concentrations in the control experiments, was strongly pH-dependent. At pH 6, $Fe(II)_{aq}$ increased throughout the whole experiment, reaching final concentrations around 1200 μM when the suspensions turned nearly transparent, implying that FeS dissolution had been almost complete. At neutral pH, $Fe(II)_{aq}$ concentrations first built up and then started to decrease after 7 d when a maximum $Fe(II)_{aq}$ concentration of 350 μM was reached. In contrast, $Fe(II)_{aq}$ concentrations at pH 8 decreased from the beginning until undetectable (<1 μM) after day 6.

The addition of P affected the temporal patterns of $Fe(II)_{aq}$ concentration significantly. The increase in $Fe(II)_{aq}$ during the first four days of reaction time was not affected by the presence of P at pH 6. However, after four days, the trend in the P treatments diverged from the control experiments and $Fe(II)_{aq}$ concentration started to decrease and remained at a constant level after about 10 d At pH 7, $Fe(II)_{aq}$ concentrations started to drop from the beginning of the experiments when P was present and reached steady state concentrations after about 3 d In contrast to the control experiments, $Fe(II)_{aq}$ concentrations stayed approximately constant or increased in the first five days at pH 8. The increase was most pronounced in experiments with initial P concentrations (P_{ini}) of 5 mM. Afterwards, the concentration decreased in the suspensions with higher P_{ini} concentrations and also reached a quasi-steady state after about 15 d

At both, pH 6 and 7, the steady state $Fe(II)_{aq}$ concentrations decreased with increasing P_{ini}. The average concentrations over the last 20 d of the experiment at pH 6 ranged between ~100 to 300 μM whereas the concentrations at pH 7 were below 100 μM. At, pH 8 the final $Fe(II)_{aq}$ concentrations only reached values between 10–40 μM. However, in contrast to the lower pH values, the $Fe(II)_{aq}$ concentrations increased with increasing P_{ini}. Irrespective of pH, elevated $Fe(II)_{aq}$ concentrations were reflected in lower contents of solid-bound Fe (Fig. S2), as expected from mass balance calculation.

With respect to the solid-bound P (P_{sb}), 4 h after the start of the experiment, higher values were measured at higher P_{ini} at all pH values. The initial P_{sb} concentration can be attributed to P adsorption onto FeS and, at given P concentration, amounts of adsorbed P were higher at pH 7 compared to the other two pH values. Irrespective of pH, P_{sb}

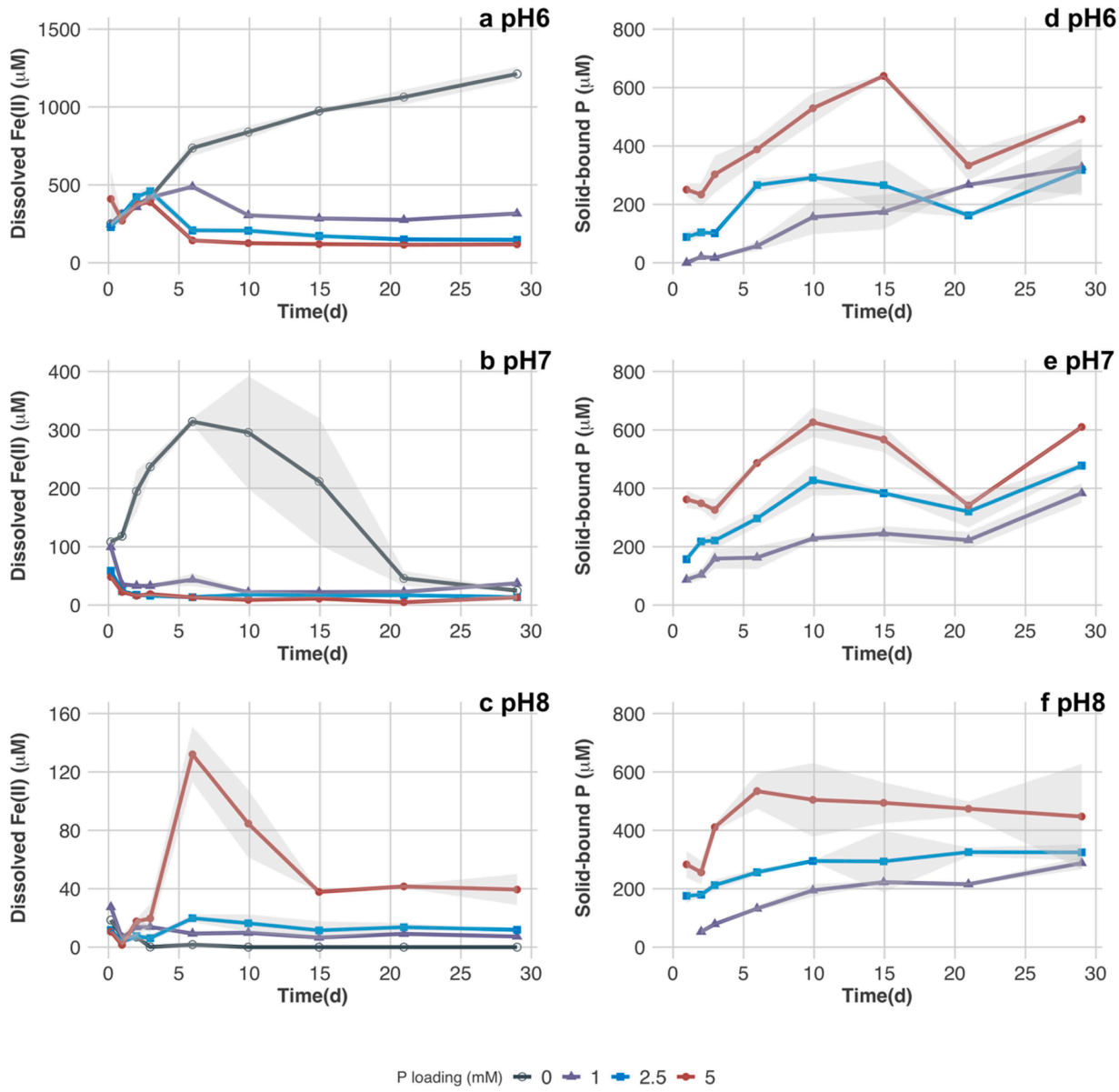

Fig. 1. Time evolution of (a, b and c) dissolved Fe(II) and (d, e and f) solid-bound phosphate concentrations at (a, d) pH 6, (b, e) pH 7 and (c, f) pH 8 for different P loading (0, 1, 2.5, and 5 mM). The shaded areas represent the minimum/maximum values for duplicate experiments. Note, the scale of the axis for dissolved Fe(II) concentrations varies between pH values. Time evolution of solid-bound Fe(II) and dissolved P are shown in Fig. S2.

concentrations showed an increasing trend during the first 10 d of the experiments, most pronounced for high P_{ini} concentrations (Fig. 1d, 1e, 1f). This increase in P_{sb} concentrations corresponded with the decrease in dissolved phosphate concentrations (P_{aq}, Fig. S2d, S2e, S2f). After 10 d, no consistent trend among the different experiments could be recognized: For P_{ini} = 1 mM, P_{sb} increased throughout the whole duration of the experiment at all pH values; for P_{ini} = 2.5 mM, P_{sb} reached steady state concentrations for pH 8 at 10 d, whereas concentrations at pH 6 & 7 fluctuated around the value measured after 10 d; and for P_{ini} = 5 mM, P_{sb} reached highest concentrations after 6 d at pH 8 and exhibited a decreasing trend afterwards. At pH 7 and 6, maximum P_{sb} concentrations appeared at 10 d and 15 d, respectively, and later for pH 8. Irrespective of the different temporal evolution, the increase in P_{sb} concentrations throughout the whole experiment was of the same range (~200 - 300 μM) for all treatments.

Dissolved S(-II) concentrations (data not shown) were low (< 50 μM) at the beginning of the experiment and usually below detection limit (<1 μM) when occasionally determined after 2 d

3.2. Solid characterization

3.4.1. X-ray diffraction (XRD)

When ignoring the background signal, all identified diffraction peaks could be ascribed to vivianite located at 13.1 (020), 11.2 (110), 18.1 (200), 21.8 (130), 23.1 (20$\bar{1}$) and 27.8 ($\bar{1}$31) 2θ Cu K-α (1.5406 Å) (Fig. 2). Although varying in relative intensity, XRD confirmed the presence of vivianite in the solids obtained from all P amended experiments, with the exception of pH 8, 1.0 mM P_{ini}. In this sample, none of the vivianite related peaks could be unequivocally identified. The intensity of the diffraction peaks was decreasing with increasing pH, most visible for the strongest diffraction at 11.2 2θ. Mackinawite could not be identified unequivocally from X-ray diffractograms and only a broad peak at 17.6 2θ could tentatively be attributed to mackinawite. No indications for the presence of other crystalline phase were obtained from XRD analysis besides a peak at around 14.2 2θ in samples from control experiments, which can be ascribed to lepidocrocite.

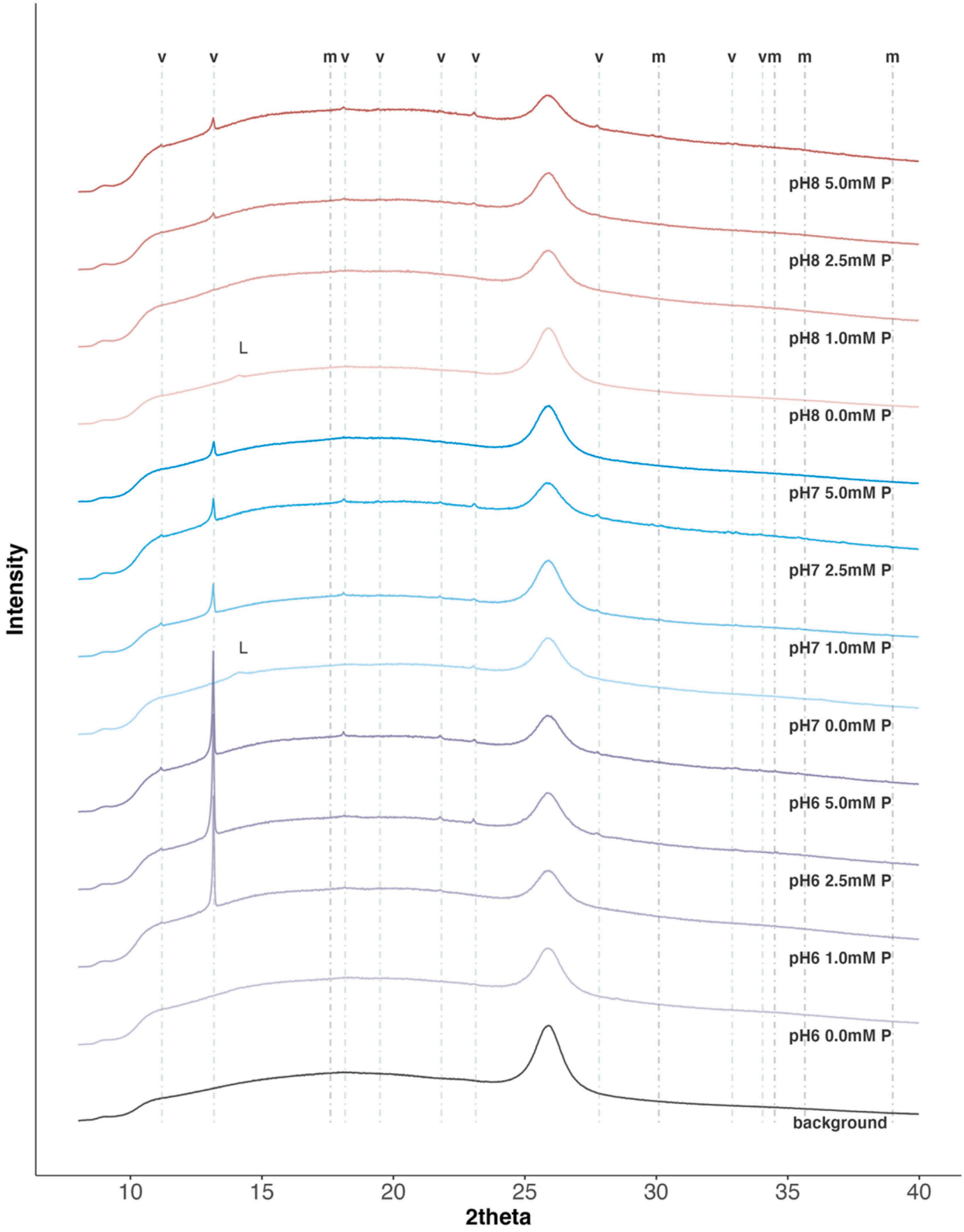

Fig. 2. X-ray diffractograms collected of solids after 37 d of reaction. The diffractograms are normalized based on the intensity of the background tape peak (at ~27° 2theta).Letters indicate diffraction peaks with high intensity of mineral standards: *v* = vivianite, *m* = mackinawite, *L*=lepidocrocite.

3.4.2. Transmission electron microscopy (TEM)

Transmission electron microscope (TEM) micrographs collected for starting material and for solids formed in the experiments with $P_{ini} = 5$ mM experiments are shown in Fig. 3. Additional images of the control experiments ($P_{ini} = 0$ mM) are provided in the Supplementary Material (Fig. S3). Particles with different morphology were observed at all pH levels for P-loaded treatments. This included particles with a size of several μm with sharp edges appearing parallelogram-shaped in the micrographs, accompanied by irregularly small particles with a size of several tenths of nm (Fig. 3a, 3b, 3c). Samples collected at pH 8 also contained particles appearing as partially wrinkled sheets. The large, parallelogram-shaped particles were absent in the starting material

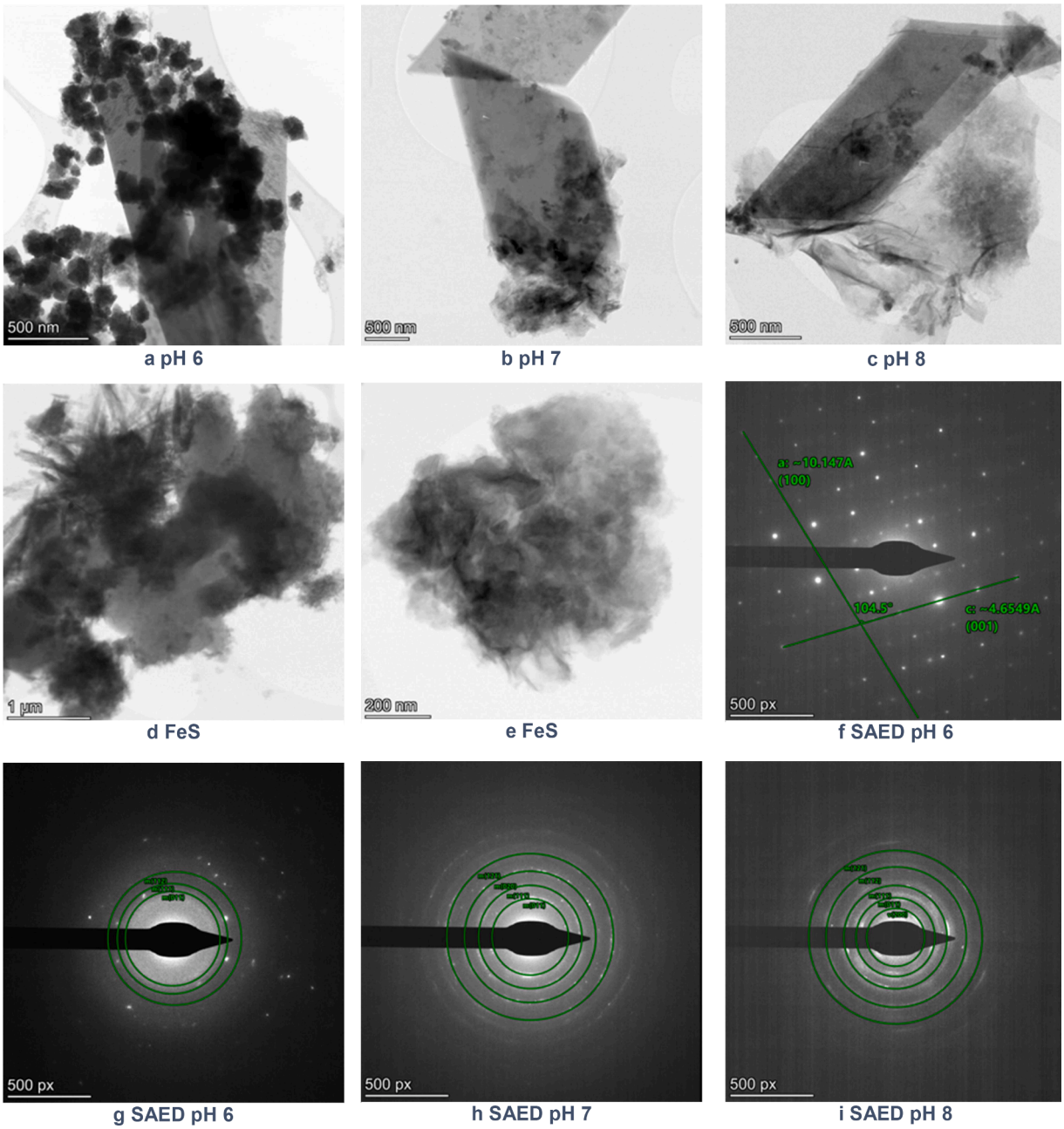

Fig. 3. Results from TEM analysis of the fresh FeS and of solids collected at the end of the experiments. Micrographs for pH 6 (a), pH 7 (b), pH 8(c) with an initial P loading of 5 mM and initial FeS (d and e); f) SEAD pattern showed a single crystalline pattern for micrograph b. g-i) g, h and i are SAED patterns taken from a, b, and c, respectively. The letters m and v at the rings in SAED figures represent diffractions, which can be attributed to mackinawite and vivianite, respectively. The corresponding EDS spectra are shown in Fig S4.

(Fig. 3d) or in the samples from control treatments (Fig. S3a, S3b, S3c) and resemble microscopic images of vivianite presented in previous studies [37,38]. Energy-dispersive X-ray spectroscopy (TEM – EDS) showed an increase in relative P contents and decrease in S(-II) signal along the trajectory from areas, which are rich in fine material, to those with the large particles (following arrow direction, Fig. S4 and Table S1). The S / Fe ratio was low (< 0.1) in general except pH 6 (~ 1.3 at spot A, Fig. S4). P / Fe ratios reached 0.6 for pH 6 and pH 7, which is within the range of the stoichiometric ratio in vivianite. Further investigation of the large particles by selective area electron diffraction (SAED) of a single particle for pH 7 underpin that the large particles are vivianite. The SAED reflect interplanar distances of 10.15 Å and 4.65 Å at an angle of 104.5° matching with the cell parameters for vivianite. Poly-crystalline diffraction patterns (pH 7 & 8, Fig. 3b and 3c) were observed and point to (011), (111), (020), and (121) planes of FeS. The 200 plane of vivianite can be attributed to the smallest circle obtained for the pH 8 sample (Fig. 3g).

3.4.3. *X-ray absorption spectroscopy*

The XANES and EXAFS spectra of all samples and of references used for the analysis of the sample spectra by LCF are shown in Figs. S6, S7, S8 and S9. Both the XANES and EXAFS spectra are analyzed by LCF (Table S2). In general, consistent results were obtained from the LCF analysis of the XANES and EXAFS spectra. To visualize the speciation of the entire Fe in all experiments, the LCF-based fractions were scaled by the fraction of solid-phase Fe (as percentage of total Fe) and are shown together with the fraction of $Fe(II)_{aq}$ in Fig. 4 (EXAFS) and Fig. S5 (XANES).

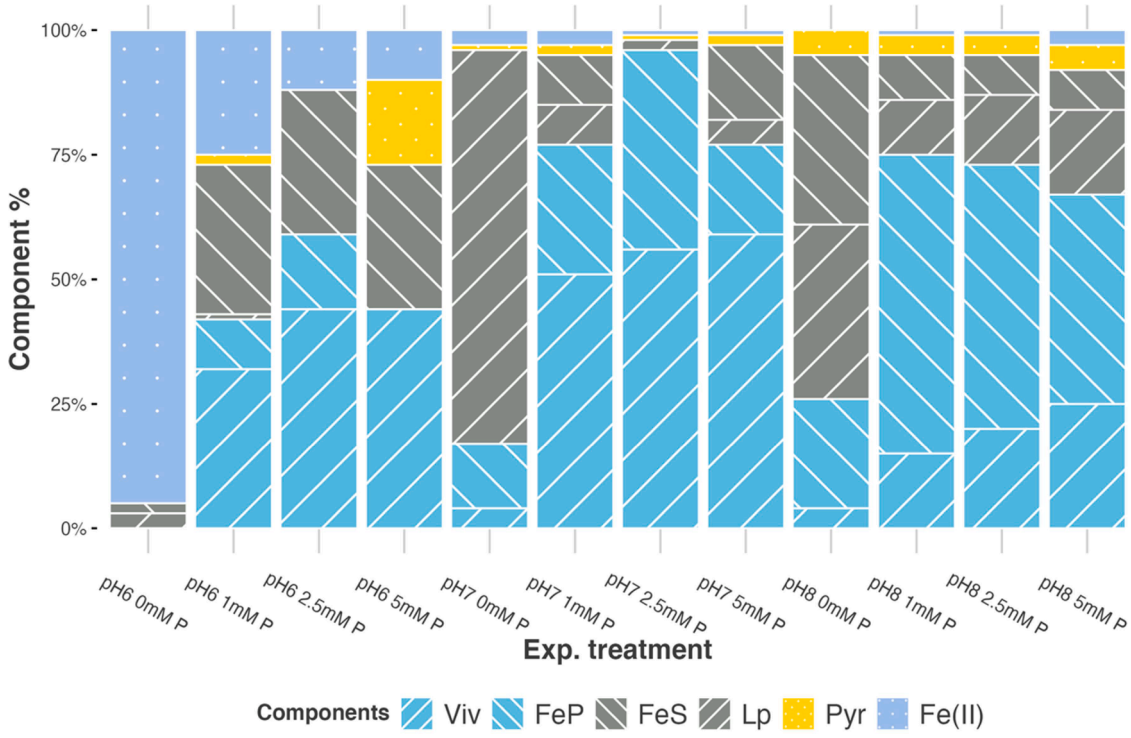

Fig. 4. Results from the LCF analysis of the Fe K-edge EXAFS spectra of solids collected on day 37 combined with data on dissolved Fe(II). The solid-phase LCF results were scaled by the fraction of solid-phase Fe as estimated from the average fractions of dissolved Fe at days 21 and 29. Viv = vivianite, FeP = amorphous basic Fe (III)-phosphate, FeS = mackinawite, Lp = lepidocrocite, Pyr = pyrite, Fe(II) = dissolved Fe(II). Corresponding results obtained from the XANES spectra are shown in Fig. S5.

The LCF analysis indicated that the samples contained between 0 and 95% ferric Fe(III), with a trend towards higher fractions in the P-free controls and at higher pH values. Considering that the analysis of total Fe(II) and total Fe in the final suspension of day 37 indicated that only a minor fraction of Fe(III) had formed by oxidation artifacts during the experiment, and that replicate samples for Mössbauer spectroscopy did not contain detectable amounts of Fe(III) (see Section 3.4.4), it was assumed that higher Fe(III) fractions observed by XAS reflected the partial oxidation of Fe in these samples during sample collection or storage in the glove box. Taking into account that mostly the lepidocrocite reference spectrum was used to account for oxidation artifacts in the P-free controls, and that the amorphous Fe(III)-phosphate reference was mainly included in the fits of spectra from P-containing treatments (Fig. 4; Table S5), it was presumed that lepidocrocite could be interpreted as a transformation artifact from mackinawite, and amorphous Fe(III)-phosphate as a transformation artifact from vivianite (considering the reported formation of amorphous Fe(III)-phosphate from vivianite, see [39]). Based on this assumption, the LCF results suggested that the extent of vivianite formation at pH 7 was higher than at pH 6 and pH 8. At pH 6, the addition of P led to the formation of vivianite at the expense of dissolved Fe^{2+}release by rapid mackinawite dissolution. Also at pH 7 and 8, the addition of P promoted the formation of vivianite. No clear trends in the extent of vivianite formation, however, were evident as a function of the concentration of P.

3.4.4. Mössbauer spectroscopy

From the analysis of the Mössbauer spectra of ^{57}Fe-labeled mackinawite reacted with 5 mM P for 29 days, no indications for the presence of ferric Fe were obtained, supporting the notion that ferric Fe in the samples analyzed by XAS was formed during sample collection or storage in the glovebox (Fig. 5). All spectra showed a mixture of paramagnetic and magnetically-ordered phases. The spectra of samples reacted at pH 7 and pH 8 are similar, and different to the spectrum of the sample reacted at pH 6. This latter spectrum was dominated by a singlet that likely corresponds to stoichiometric mackinawite [40]. The absorption near ~3 mm/s suggests the presence of more than one doublet. Hyperfine parameters of the two doublets correspond well to Fe(II) in vivianite, including a roughly 2:1 area ratio [41]. The six-line signals (sextets) near 6 mm/s indicated greigite formation [42] (in qualitative agreement with a relatively high fraction of pyrite in the sample reacted at pH 6 at 5 mM P), and the remaining sextet is likely Fe_xS [40]. Spectra at pH 7 and pH 8 were dominated by an asymmetric sextet, corresponding to mackinawite with excess S. Vivianite formation is consistent with the remaining absorption. At pH 7 and pH 8, the extent of vivianite formation was ~20% (less than obtained by XAS on a different set of samples) and the remaining Fe was attributed to mackinawite with excess S. For pH 6, ~30% transformed into vivianite, and 17% into greigite. The distribution of iron in the different phases is summarized in Table 1 and hyperfine parameters are listed in Table S3.

4. Discussion

4.1. Verification of FeS transformation into vivianite and underlying mechanism

XRD, Mössbauer, XAS and TEM analyses unisonously corroborate the formation of vivianite in all P-amended treatments. Hence, the results provide direct evidence that transformation of FeS into vivianite can be an effective pathway to immobilize dissolved P. For example, for P_{ini} = 1 mM, final P_{aq} concentrations reached about 476, 390, 750 μM for pH 6, 7 and 8, respectively. The formation of vivianite has been expedited in the experiments due to relatively high P_{aq} concentrations from 1 to 5 mM. However, P concentrations of hundreds of μM up to 1 mM are not uncommon in pore waters of marine and freshwater sediments [43–45] implying that FeS can also be an effective Fe source for vivianite formation in aquatic sediments. The time evolution of the $Fe(II)_{aq}$ concentration at pH 6 is in line with the expectations based on the hypothesis. The initial increase in $Fe(II)_{aq}$ concentration is reflecting

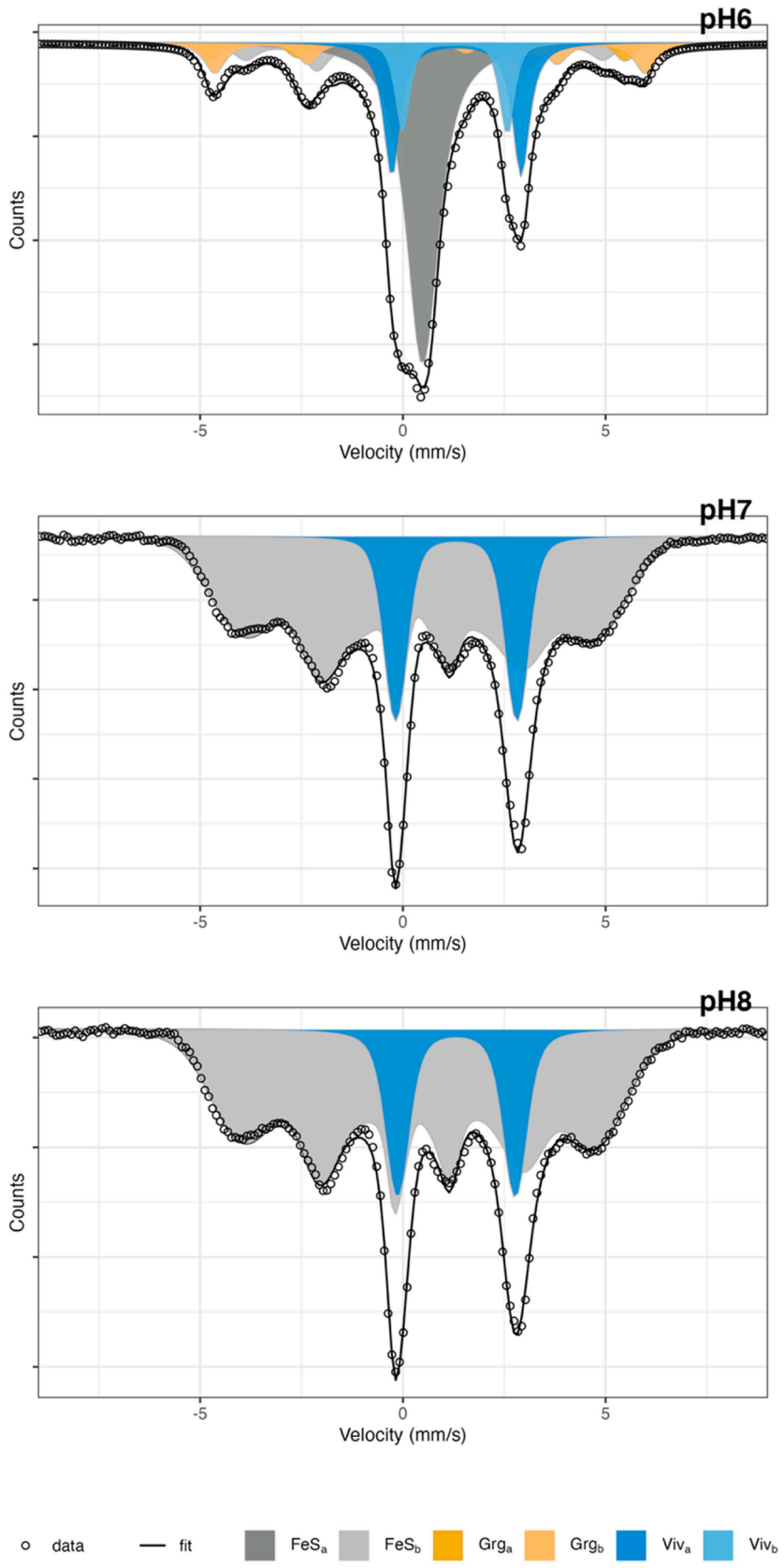

Fig. 5. Mössbauer spectra of ^{57}Fe labeled mackinawite reacted with 5 mM P for 29 days. The spectra were recorded at ~ 80 K. FeS$_{a,b}$ = mackinawite, Grg$_{a,b}$ = greigite, Viv$_{a,b}$ = vivianite. Corresponding parameters used for fitting are listed in Table S3.

Table 1
Distribution of iron in the different phases from Mössbauer spectra.

Treatment	Speciation (%)			
	Stoichiometric mackinawite	Vivianite	Greigite	Unidentified iron sulfide
pH 6	43	29	17	11
pH 7	79	21		
pH 8	81	19		

relatively fast FeS dissolution, the subsequent decline in $Fe(II)_{aq}$, accompanied with an increase in P_{sb}, can be ascribed to vivianite precipitation (Fig. 1). This implies that FeS dissolution is a prerequisite for vivianite formation and that vivianite forms via a dissolution – precipitation process. The different morphologies of FeS and vivianite, observed in the TEM micrographs, further supports the dissolution – precipitation pathway. At pH 6, the transition from increasing to decreasing $Fe(II)_{aq}$ occurs after about 4–6 days when saturation indices for vivianite reached values between 3 and 4 (Fig. 6). This corresponds with the observation of rapid vivianite nucleation and precipitation at SI values >4 [23].

The trend in $Fe(II)_{aq}$ after 4–6 days, further indicates that $Fe(II)_{aq}$ consumption due to vivianite formation proceeds faster than FeS dissolution beyond this time, implying that vivianite growth becomes limited by the rates of Fe supply from FeS dissolution. The phase of vivianite growth limitation by FeS dissolution extends until the end of the experiment, with SI values remaining close to 2.0. This is also in agreement with the assessment of reported rates for FeS dissolution and vivianite growth reported in literature and presented in the introduction. That is, vivianite growth rates are strongly depending on the distance from equilibrium, reflected in the SI value, and are expected to surpass FeS dissolution rates at SI values between 2.0 and 4.0.

The SI values do not fall below 2.0 in the experiments at pH 6 implying that the solutions do not reach equilibrium with respect to vivianite. This can be explained by a strong dependency of the vivianite growth rates on SI as reported by Madsen and Hansen, [21]. Only a marginal decrease in SI is sufficient for vivianite growth rates to follow the decline in FeS dissolution rates towards the end of the experiment. At lower SI values, the reaction becomes so slow that equilibrium is not reached over the duration of the experiment.

The temporal evolution of $Fe(II)_{aq}$ in the experiments at pH 7 and pH 8 deviates from that observed at pH 6 in a number of ways: there is no initial increase in $Fe(II)_{aq}$ concentration in the P amended suspensions, and $Fe(II)_{aq}$ concentrations do not increase in control experiments (pH 8) or the increase is not prolonged over the whole experiment (pH 7). This implies that the mechanism of vivianite formation from FeS cannot be directly deduced from the temporal evolution of solution composition at these pH values. However, the similarity in size and shape of vivianite crystals formed at all pH values suggests that it was formed via the same reaction sequence at all pH values. The absence of an initial $Fe(II)_{aq}$ increase, as observed in the P-amended suspensions at pH 7 and 8, can be attributed to the relative high initial SI > 4.0 that ensures rapid vivianite nucleation and growth [23].

4.2. *Effect of p_{ini} and pH on the rates and extent of vivianite formation from FeS*

Based on the conclusion that vivianite formation proceeds via dissolution and precipitation and that the transformation is limited by FeS dissolution rates, it is expected that the effect of pH and P concentration on FeS dissolution rates is reflected in the rates and consequently the extent of vivianite formation. At pH 6 initial rates of $Fe(II)_{aq}$ production (Table 2) are similar in control and P amended experiments, implying that P concentrations do not significantly affect FeS dissolution rates at pH 6. For the first 3 days of reaction, the average rate of $Fe(II)_{aq}$ production is about 67 $\mu M\ d^{-1}$. Based on the rate law by Pankow and Morgan [20] and assuming a specific surface area of 350 m^2/g [25] for FeS, $Fe(II)_{aq}$ rates around 1.0 $M\ d^{-1}$ would be expected, which are more than three orders of magnitude larger than those observed in our experiments. The considerable difference can be partially attributed to the

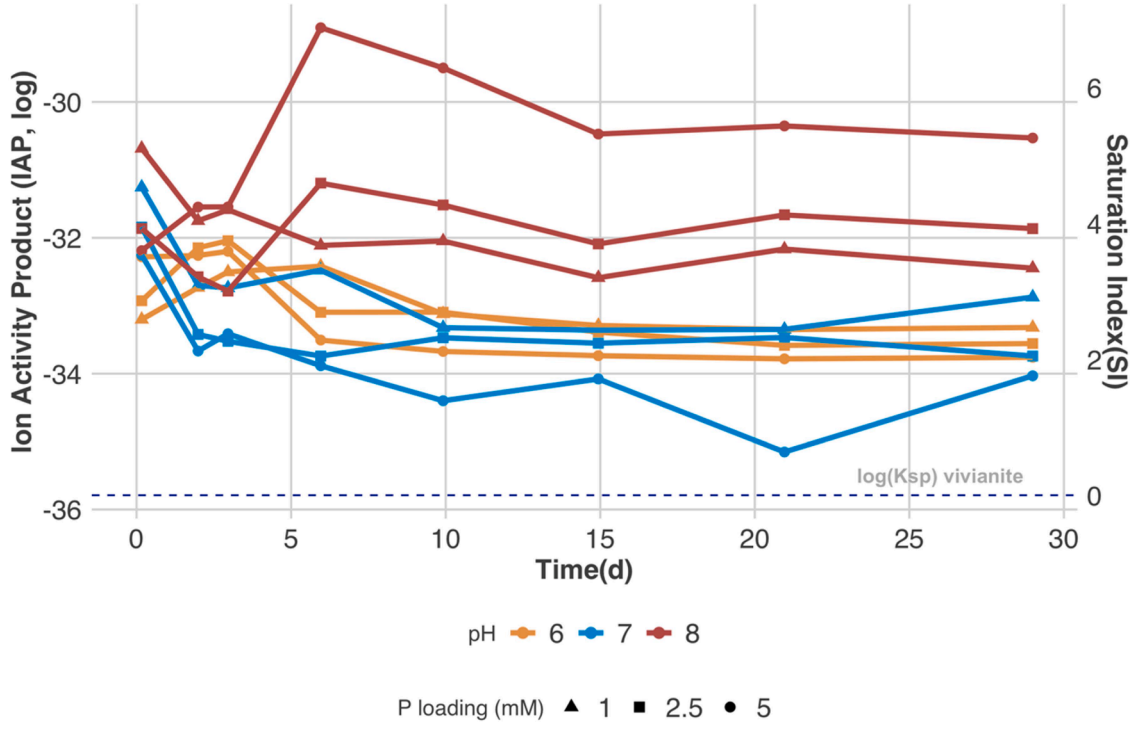

Fig. 6. Time evolution of ion activity products (IAP, left, in logarithm scale) and corresponding saturation indices (SI, right). Values are calculated based on the concentrations of dissolved Fe and P and the suspension pH. The dashed blue line indicates the solubility product of vivianite [36]. Values were calculated based on the average measured concentration of duplicate experiments.

Table 2
$Fe(II)_{aq}$ production rates due to FeS dissolution and P_{sb} production rate.

Treatment		$Fe(II)_{aq}$ production rate				P_{sb} production rate			
pH	P_{ini}(mM)	rate(μM/d)	Std. E	R^2	Fit for period (day)	rate(μM/d)	Std. E	R^2	Fit for period (day)
6	0	83.0	7.5	0.976	0–6				
6	1	40.6	6.2	0.935	0–6	12.6	1.7	0.941	5–15
6	2.5	85.6	11.6	0.965	0–4	−0.2	9.0	0.895	5–15
6	5	60.4	25.2	0.852	0–4*	27.7	2.0	0.984	5–15
7	0	83.0	7.5	0.976	0–6				
7	1					14.5	2.9	0.896	0–10
7	2.5					28.4	2.2	0.983	0–10
7	5					33.3	5.9	0.914	0–10
8	0								
8	1					19.5	1.8	0.992	0–6
8	2.5					17.0	2.3	0.964	0–6
8	5					55.7	14.5	0.881	0–6

* the first data point removed since it is an outliner.

underestimation of the reactive interface in the study by Pankow and Morgan, [20], who only considered the surface area of a pressed pellet and not the surface of individual particles inside the pellet, but this cannot explain several orders of magnitude discrepancy. After 3 days of reaction, the pace of FeS dissolution in control experiments slows down and, once vivianite formation is initiated, the progress of FeS dissolution cannot be calculated any more based on $Fe(II)_{aq}$ trends in P containing experiments. However, FeS dissolution rates can be deduced from the rates of P_{sb} production assuming that P_{sb} increase can be exclusively attributed to vivianite formation and is mostly coupled to the consumption of P_{aq} and not on the expense of P adsorbed onto FeS. Calculating the rates based on the change in P_{sb} concentration in the period 7–15 days, when $Fe(II)_{aq}$ concentrations are steady, yields and average rate of 23 μM d^{-1} (Table 2). This value is in accordance with the rates of $Fe(II)_{aq}$ production in the control experiments during this period (around 40 μM d^{-1}) when taking into consideration the stoichiometry of vivianite. Hence, once initiated, vivianite growth follows the progress of FeS dissolution in the first 10-–15 days of the experiment and no indications for a dependency of the rates of FeS dissolution on the presence of P are given. Note, as sulfide is disappearing from reactor throughout the experiment, the determined rates represent far-from-equilibrium rates. The dissolution likely proceeds slower when dissolved sulfide would accumulate in the solution and is not consumed. When extrapolating the initial rates of FeS dissolution and in view of the extent of FeS dissolution in the control experiment, all initially added FeS should be transformed into vivianite in all P amended experiments. However, the EXAFS-based LCF results suggested that only between 55 and 97% of the total Fe (72% ± 14%, $n = 9$) were transformed into vivianite (when interpreting amorphous Fe(III)-phosphate as oxidation artifact of vivianite), which also tentatively corresponds to estimations based on the change in P_{sb} concentration, at the end of the experiment (Table S5). This implies that the formation of vivianite with Fe from mackinawite becomes impeded in the later stage of the experiment, as further discussed in the next section.

At pH 7, the initial rates of $Fe(II)_{aq}$ production in the control experiment as well as the rates of P_{sb} production are comparable to those obtained at pH 6, implying that FeS dissolution rates are similar at these two pH values. This is in line with the rate measurements of FeS solution in buffered solutions around pH 6 and pH 7 [20]. However, in contrast to pH 6, the systematic increase in P_{sb} production rates with increasing P_{ini} concentrations indicates that vivianite formation, and hence FeS dissolution, proceeds faster with increasing phosphate concentration. This could be ascribed to ligand-promoted dissolution as reported for the influence of P adsorption on the dissolution of Fe(III) hydr(oxides) at low pH, when monodentate surface complexes of P prevail [46]. Conversely, arsenic adsorption onto FeS inhibits its transformation into pyrite [47] but for arsenate the influence is more complex as it also undergoes redox reactions with FeS. Nevertheless, in analogy to the effect of arsenite on FeS transformation into pyrite vivianite formation by P could also be explained by its inhibitory effect on FeS aging (see following section).

P-promoted formation of vivianite with Fe from mackinawite is further corroborated by the results from experiments at pH 8. In the control experiment, $Fe(II)_{aq}$ concentrations stay at very low levels and no indications for FeS dissolution are given. Pankow and Morgan [20] did not investigate FeS dissolution at pH values above 7.0. However, FeS dissolution did not exhibited a strong pH-dependency between 4 - 7. Hence, the non-appearance of FeS dissolution in control experiments is surprising. We hypothesis that the absence of $Fe(II)_{aq}$ production at pH 8 can be caused by a pH dependence of FeS aging. That is, FeS aging might be proceeding faster at pH 8 than at lower pH values, leading to the formation of a more stable sulfide phase, which dissolves in a much lower pace. Despite absence FeS dissolution in the control experiments, considerable amounts of vivianite are formed. When attributing lack of FeS dissolution due to aging, the enhancing effect of P_{ini} on vivianite formation can be ascribed to its inhibitory effect on FeS aging. In contrast to lower pH values, $Fe(II)_{aq}$ concentrations after 7 d reaction time are higher at higher P_{ini} levels. Formation of aqueous Fe^{2+}-P complexes can account for the increase in $Fe(II)_{aq}$ concentrations with increasing P_{ini}. Based on equilibrium calculations, however, the fraction of aqueous Fe^{2+}-P complexes, at given $Fe(II)_{aq}$ and total P concentration, only marginally increases from pH 6 to pH 8. Therefore, it appears unlikely that pH dependency on Fe speciation explains the changing trend in $Fe(II)_{aq}$ concentration as a function of P_{ini} with increasing pH. Consequently, it is more likely that the presence of P at pH 8 increases the mobilization of Fe from FeS by retarding its aging and, by this, facilitating Fe mobilization and, consequently, vivianite formation.

4.3. Limitations of vivianite formation due to FeS aging

Incomplete formation of vivianite with Fe from mackinawite over the duration of the experiment can be explained by aging of the freshly precipitated FeS. Aging of freshly precipitated FeS at room temperature, under strict anaerobic conditions and in the presence of excess H_2S, leads to the formation of crystalline FeS within the time scale of weeks and months [48,49]. However, in the absence of excess H_2S and in the presence of small amounts of oxygen or sulfur, greigite, pyrite and elemental sulfur are also formed. Despite all precautions, we cannot exclude the invasion of some oxygen into the sampling bottles during sampling of the experimental suspensions, implying that FeS transformation could be partially triggered by oxidation. Oxidation, could also partially explain the decrease in $Fe(II)_{aq}$ concentrations in control experiments at pH 7 between 5 and 20 days reaction time. However, dedicated analyses to determine the fraction of solid-bound Fe(III) at the end of the experiment revealed, that the fraction of Fe(III) was, with the exception of control experiments at pH 6, below 10% (Table S4). The Fe (III) contents were generally higher than expected based on residual dissolved oxygen concentrations after N_2 purging, as stated by Butler

et al. [24] (less than 0.3% of total Fe). This indicates that oxygen intrusion during sampling was the dominant source of oxidation artifacts. Presence of greigite or pyrite could not be inferred based on the XRD analyses but some greigite was found in the pH 6 sample prepared for Mössbauer analysis. Furthermore, the appearance of platy particles in the TEM micrographs of control samples also point towards the presence of greigite. Consequently, crystallization of amorphous FeS and possibly some greigite is presumable the main process competing with vivianite precipitation and leading to incomplete transformation into vivianite over the duration of the experiments.

The effect of P on FeS aging and its pH dependency can explain the lower extent of vivianite formation at pH 8 compared to the other pH values. Faster aging of amorphous FeS at pH 8 can be possibly ascribed to the speciation of dissolved S(-II): supersaturation with respect to crystalline FeS requires lower levels of dissolved S(-II) at pH 8 than at lower pH values. The dependency of vivianite formation on P_{ini} can be correspondingly explained by the retardation of FeS aging by P adsorption. FeS transformation was found to be slowed down in the presence of arsenic [50]. Analogically, it is therefore possible that P adsorption also reduces the aging process of FeS. This is supported by TEM analysis, as the sheet-like structure of amorphous FeS appears to be better preserved in the presence of P, in particular at pH 8. Higher adsorption of P on FeS with increasing P_{ini} is reflected in increasing P/Fe ratios in the solids with increasing P_{ini}, at the beginning of the experiment with little or no vivianite formation (Fig. 7).

4.4. Implications

Unambiguous identification of vivianite in aquatic sediments is often challenging as vivianite often only comprises a small part of the sedimentary Fe and P pools. Frequently applied sequential extraction schemes for Fe and P do not specifically target vivianite and detection of vivianite often requires specific approaches such as spectroscopic techniques or density separation [3]. The latter implies that vivianite is usually only found when specifically looked for. Vivianite is generally not expected in sulfidic environments and anoxic marine sediments in general, due to the high sulfate concentrations in sea water. Furthermore, authigenic apatite formation, considered the most important authigenic P mineral in marine sediments [51], can constrain the availability of P for vivianite formation. Nevertheless, formation of vivianite can be favored in organic-rich sediments below the sulfate / methane transition zone when the produced S(-II) becomes precipitated [9,45,52]. Egger et al. [8] concluded for sediments in the Bothnian Sea that Fe(II) required for vivianite precipitation is produced by anoxic methane oxidation coupled to iron reduction. Our study indicates that also mackinawite dissolution can provide the required Fe(II) for vivianite precipitation in a setting where S(-II) production is limited and S(-II) is removed by transport or reactions, such as oxidation. Taking this pathway into account might open new perspectives for investigating the role of vivianite for P burial in aquatic sediments, which has not been considered so far. Aging of mackinawite, however, can obstruct the transformation into vivianite by leading to slower dissolution rates. Here, we obtained indications that P adsorption can inhibit the aging but it might be possible that adsorption or co-precipitation of other constituents, e.g. organic matter and calcium as reported for the aging of P containing Fe(III) precipitates [53], can also retard or inhibit FeS aging. To our knowledge, the effect of organic matter or electrolyte composition on FeS aging has not been systematically investigated but might be key in assessing the importance of FeS to vivianite formation in natural, aquatic sediments. Beyond phosphate burial in aquatic sediments, vivianite from FeS could also hold implications in engineering applications. Iron addition is frequently applied for sulfide control in sewers and digesters. The formed FeS could then form an iron source for vivianite formation when sulfide levels decrease and phosphate concentrations increase due to progressive mineralization of organic matter. Vivianite has been identified as a major P precipitate in sewage treatment plants and can be easily recovered using magnetic methods [54].

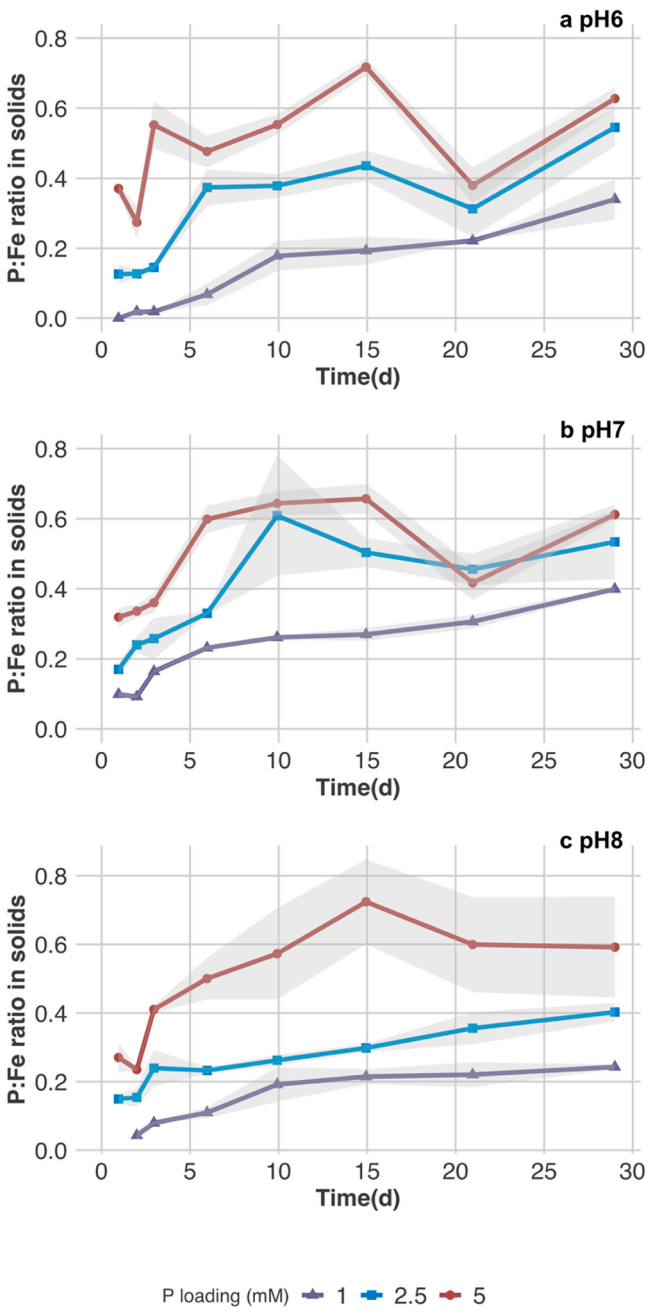

Fig. 7. Time evolution of P/Fe ratio in solids obtained with different initial P loading: a) pH 6, b) pH 7 and c) pH 8. The values were calculated based on the average contents obtained from duplicate experiments. The shaded area represents the minimum/maximum values for duplicates.

5. Conclusion

This study provides experimental evidence that amorphous FeS can be an effective Fe source for authigenic vivianite formation. The transformation proceeds via a dissolution- precipitation mechanism. Once moderate supersaturation is reached, the Fe supply via FeS dissolution is the rate limiting step. Aging of amorphous FeS that leads to the formation of more crystalline mackinawite or possibly other crystalline Fe sulfides can compete with vivianite formation. That is because the transformation products limit $Fe(II)_{aq}$ levels due to their higher thermodynamic stability and/or lower dissolution rates in case that vivianite

formation is thermodynamically still feasible. This implies that authigenic vivianite formation can be fueled by the dissolution of amorphous FeS in aquatic sediments and represents a pathway for P burial in sediments, in which vivianite is usually not considered.

Funding

This work was supported by the European Union's Horizon 2020 research and innovation program under the Marie Skłodowska-Curie grant agreement No 813438.

Appendix A. Supplementary Material

Supplementary material provides a collection of figures (Figs. S1-S9) and tables (Tables S1-S5) discussed in the manuscript. Specifically, equilibrium calculation for expected vivianite concentration is presented in Fig. S1. Fig. S2 reports on time evolution of solid-bound Fe(II) and dissolved P concentration. Figs. S3–4 and Table S1 contain additional information on TEM results, and Figs. S5–9 provide the LCF fitting results for XANES, along with original, fitted and reference spectra for XAS results. Tables S3–5 summarize the parameters for Mössbauer fitting, the final check of Fe(II) concentration, and a comparison of expected vivianite transformation extent between wet chemistry results and EXAFS fitting.

Declaration of Competing Interest

The authors declare that they have no known competing financial interests or personal relationships that could have appeared to influence the work reported in this paper.

Data availability

I have shared the link to my data at the attach file step. FeS2viv_Ma_etal_2023

Acknowledgement

This study was funded by "P-TRAP" (EU Grant No. 813438, Marie Skłodowska- Curie Actions). We would like to thank Dr. Oliver Plümper and Dr. Maartje Hamers for the access to and operation of TEM measurements at the electron microscope center of UU. Discussions with Prof. Stefan Peiffer were appreciated.

Supplementary materials

Supplementary material associated with this article can be found, in the online version, at doi:10.1016/j.ceja.2023.100565.

References

[1] F.A. Khan, A.A. Ansari, Eutrophication: an ecological vision, Bot. Rev. 71 (2005) 449–482.
[2] J.O. Nriagu, Stability of vivianite and ion-pair formation in the system $Fe_3(PO_4)_2$-H_3PO_4-H_2O, Geochim. Cosmochim. Acta 36 (1972) 459–470.
[3] M. Rothe, A. Kleeberg, M. Hupfer, The occurrence, identification and environmental relevance of vivianite in waterlogged soils and aquatic sediments, Earth-Sci. Rev. 158 (2016) 51–64.
[4] F.J.H. Mackereth, Some chemical observations on post-glacial lake sediments, Philos. Trans. R. Soc. Lond. B. Biol. Sci. 250 (1966) 165–213.
[5] L. Heinrich, M. Rothe, B. Braun, M. Hupfer, Transformation of redox-sensitive to redox-stable iron-bound phosphorus in anoxic lake sediments under laboratory conditions, Water Res. 189 (2021), 116609.
[6] M. Rothe, T. Frederichs, M. Eder, A. Kleeberg, M. Hupfer, Evidence for vivianite formation and its contribution to long-term phosphorus retention in a recent lake sediment: a novel analytical approach, Biogeosciences 11 (2014) 5169–5180.
[7] N. Dijkstra, C.P. Slomp, T. Behrends, Vivianite is a key sink for phosphorus in sediments of the Landsort Deep, an intermittently anoxic deep basin in the Baltic Sea, Chem. Geol. 438 (2016) 58–72.
[8] M. Egger, T. Jilbert, T. Behrends, C. Rivard, C.P. Slomp, Vivianite is a major sink for phosphorus in methanogenic coastal surface sediments, Geochim. Cosmochim. Acta 169 (2015) 217–235.
[9] C. März, J. Hoffmann, U. Bleil, G.J. de Lange, S. Kasten, Diagenetic changes of magnetic and geochemical signals by anaerobic methane oxidation in sediments of the Zambezi deep-sea fan (SW Indian Ocean), Mar. Geol. 255 (2008) 118–130.
[10] R.A. Berner, Stability fields of iron minerals in anaerobic marine sediments, J. Geol. 72 (1964) 826–834.
[11] S. Olsson, J. Regnéll, A. Persson, P. Sandgren, Sediment-chemistry response to land-use change and pollutant loading in a hypertrophic lake, southern Sweden, J. Paleolimnol. 17 (1997) 275–294.
[12] M. Rothe, A. Kleeberg, B. Grüneberg, K. Friese, M. Pérez-Mayo, M. Hupfer, Sedimentary sulphur: iron ratio indicates vivianite occurrence: a study from two contrasting freshwater systems, PLoS ONE 10 (2015), e0143737.
[13] A. Vuillemin, D. Ariztegui, A.S. De Coninck, A. Lücke, C. Mayr, C.J. Schubert, Origin and significance of diagenetic concretions in sediments of Laguna Potrok Aike, southern Argentina, J. Paleolimnol. 50 (2013) 275–291.
[14] S. Emerson, G. Widmer, Early diagenesis in anaerobic lake sediments-II. Thermodynamic and kinetic factors controlling the formation of iron phosphate, Geochim. Cosmochim. Acta 42 (1978) 1307–1316.
[15] C. Pfeffer, S. Larsen, J. Song, M. Dong, F. Besenbacher, R.L. Meyer, K.U. Kjeldsen, L. Schreiber, Y.A. Gorby, M.Y. El-Naggar, K.M. Leung, A. Schramm, N. Risgaard-Petersen, L.P. Nielsen, Filamentous bacteria transport electrons over centimetre distances, Nature 491 (2012) 218–221.
[16] A.J. Kessler, M. Wawryk, U. Marzocchi, K.L. Roberts, W.W. Wong, N. Risgaard-Petersen, F.J.R. Meysman, R.N. Glud, P.L.M. Cook, Cable bacteria promote DNRA through iron sulfide dissolution, Limnol. Oceanogr. 64 (2019) 1228–1238.
[17] T. Sandfeld, U. Marzocchi, C. Petro, A. Schramm, N. Risgaard-Petersen, Electrogenic sulfide oxidation mediated by cable bacteria stimulates sulfate reduction in freshwater sediments, ISME J. 14 (2020) 1233–1246.
[18] F. Sulu-Gambari, D. Seitaj, T. Behrends, D. Banerjee, F.J.R. Meysman, C.P. Slomp, Impact of cable bacteria on sedimentary iron and manganese dynamics in a seasonally-hypoxic marine basin, Geochim. Cosmochim. Acta 192 (2016) 49–69.
[19] A.C. Lasaga, Kinetic Theory in the Earth Sciences, Princeton university press, Princeton, New Jersey, 1998.
[20] J.F. Pankow, J.J. Morgan, Dissolution of tetragonal ferrous sulfide (mackinawite) in anoxic aqueous systems. 1. Dissolution rate as a function of pH, temperature, and ionic strength, Environ. Sci. Technol. 13 (1979) 1248–1255.
[21] H.E.L. Madsen, H.C.B. Hansen, Kinetics of crystal growth of vivianite, $Fe_3(PO_4)_2 \cdot 8H_2O$, from solution at 25, 35 and 45°C, J. Cryst. Growth 401 (2014) 82–86.
[22] P.V. Cappellen, R.A. Berner, Fluorapatite crystal growth from modified seawater solutions, Geochim. Cosmochim. Acta 55 (1991) 1219–1234.
[23] J. Liu, X. Cheng, X. Qi, N. Li, J. Tian, B. Qiu, K. Xu, D. Qu, Recovery of phosphate from aqueous solutions via vivianite crystallization: thermodynamics and influence of pH, Chem. Eng. J. 349 (2018) 37–46.
[24] I.B. Butler, M.A.A. Schoonen, D.T. Rickard, Removal of dissolved oxygen from water: a comparison of four common techniques, Talanta 41 (1994) 211–215.
[25] M. Wolthers, S.J. Van Der Gaast, D. Rickard, The structure of disordered mackinawite, Am. Mineral. 88 (2003) 2007–2015.
[26] L.P. Nielsen, N. Risgaard-Petersen, H. Fossing, P.B. Christensen, M. Sayama, Electric currents couple spatially separated biogeochemical processes in marine sediment, Nature 463 (2010) 1071–1074.
[27] S. Fonselius, D. Dyrssen, B. Yhlen, Determination of hydrogen sulphide, in: K. Grasshoff, K. Kremling, M. Ehrhardt (Eds.), Methods of Seawater Analysis, Wiley-VCH Verlag GmbH, Weinheim, Germany, 1999, pp. 91–100.
[28] E. Viollier, P.W. Inglett, K. Hunter, A.N. Roychoudhury, P. Van Cappellen, The ferrozine method revisited: fe(II)/Fe(III) determination in natural waters, Appl. Geochem. 15 (2000) 785–790.
[29] H.P. Hansen, F. Koroleff, Determination of nutrients, in: K. Grasshoff, K. Kremling, M. Ehrhardt (Eds.), Methods of Seawater Analysis, Wiley-VCH Verlag GmbH, Weinheim, Germany, 1999, pp. 159–228.
[30] A.C. Senn, R. Kaegi, S.J. Hug, J.G. Hering, S. Mangold, A. Voegelin, Composition and structure of Fe(III)-precipitates formed by Fe(II) oxidation in water at near-neutral pH: interdependent effects of phosphate, silicate and Ca, Geochim. Cosmochim. Acta 162 (2015) 220–246.
[31] B. Ravel, M. Newville, *ATHENA, ARTEMIS, HEPHAESTUS* : data analysis for X-ray absorption spectroscopy using *IFEFFIT*, J. Synchrotron Radiat. 12 (2005) 537–541.
[32] M. Wan, C. Schröder, S. Peiffer, Fe(III):S(-II) concentration ratio controls the pathway and the kinetics of pyrite formation during sulfidation of ferric hydroxides, Geochim. Cosmochim. Acta 217 (2017) 334–348.
[33] C. Prescher, C. McCammon, L. Dubrovinsky, *MossA* : a program for analyzing energy-domain Mössbauer spectra from conventional and synchrotron sources, J. Appl. Crystallogr. 45 (2012) 329–331.
[34] K. Lagarec, D.G. Rancourt. Recoil User Manual—Mossbauer Spectral Analysis Software for Windows, University of, Ottawa. Ottawa, Canada, 1998.
[35] Gustafsson J.P., 2020. Visual MINTEQ (Version 3.1). https://vminteq.com/.
[36] A. Al-Borno, M.B. Tomson, The temperature dependence of the solubility product constant of vivianite, Geochim. Cosmochim. Acta 58 (1994) 5373–5378.
[37] M. Sánchez-Román, F. Puente-Sánchez, V. Parro, R. Amils, Nucleation of Fe-rich phosphates and carbonates on microbial cells and exopolymeric substances, Front. Microbiol. 6 (2015) 1–9.
[38] Q. Yuan, S. Wang, X. Wang, N. Li, Biosynthesis of vivianite from microbial extracellular electron transfer and environmental application, Sci. Total Environ. 762 (2021), 143076.
[39] G. Pratesi, C. Cipriani, G. Giuli, W.D. Birch, Santabarbaraite: a new amorphous phosphate mineral, Eur. J. Mineral. (2003) 185–192.

[40] C. Schröder, M. Wan, I.B. Butler, A. Tait, S. Peiffer, C.A. McCammon, Identification of mackinawite and constraints on its electronic configuration using Mössbauer spectroscopy, Minerals 10 (2020) 1090.
[41] G. Amthauer, G.R. Rossman, Mixed valence of iron in minerals with cation clusters, Phys. Chem. Miner. 11 (1984) 37–51.
[42] R.E. Vandenberghe, E. de Grave, P.M.A. de Bakker, M. Krs, J.J. Hus, Mössbauer effect study of natural greigite, Hyperfine Interact 68 (1992) 319–322.
[43] B.O. Isiuku, C.E. Enyoh, Pollution and health risks assessment of nitrate and phosphate concentrations in water bodies in South Eastern, Nigeria, Environ. Adv. 2 (2020), 100018.
[44] K.C. Ruttenberg, Development of a sequential extraction method for different forms of phosphorus in marine sediments, Limnol. Oceanogr. 37 (1992) 1460–1482.
[45] C.P. Slomp, H.P. Mort, T. Jilbert, D.C. Reed, B.G. Gustafsson, M. Wolthers, Coupled dynamics of iron and phosphorus in sediments of an oligotrophic coastal basin and the impact of anaerobic oxidation of methane, PLoS ONE 8 (2013) e62386.
[46] G. Bondietti, J. Sinniger, W. Stumm, The reactivity of Fe(III) (hydr)oxides: effects of ligands in inhibiting the dissolution, Colloids Surf. Physicochem. Eng. Asp. 79 (1993) 157–167.
[47] M. Wolthers, L. Charlet, C.H. van Der Weijden, P.R. van der Linde, D. Rickard, Arsenic mobility in the ambient sulfidic environment: sorption of arsenic(V) and arsenic(III) onto disordered mackinawite, Geochim. Cosmochim. Acta 69 (2005) 3483–3492.
[48] L.G. Benning, R.T. Wilkin, H.L. Barnes, Reaction pathways in the Fe-S system below 100°C, Chem. Geol. 167 (2000) 25–51.
[49] D. Csákberényi-Malasics, J.D. Rodriguez-Blanco, V.K. Kis, A. Rečnik, L.G. Benning, M. Pósfai, Structural properties and transformations of precipitated FeS, Chem. Geol. 294–295 (2012) 249–258.
[50] M. Wolthers, I.B. Butler, D. Rickard, Influence of arsenic on iron sulfide transformations, Chem. Geol. 236 (2007) 217–227.
[51] K.C. Ruttenberg, The global phosphorus cycle, Treatise on Geochem. 8 (2003) 682.
[52] T. Jilbert, C.P. Slomp, Iron and manganese shuttles control the formation of authigenic phosphorus minerals in the euxinic basins of the Baltic Sea, Geochim. Cosmochim. Acta 107 (2013) 155–169.
[53] V.V. Nenonen, R. Kaegi, S.J. Hug, J. Göttlicher, S. Mangold, L.H.E. Winkel, A. Voegelin, Formation and transformation of Fe(III)- and Ca-precipitates in aqueous solutions and effects on phosphate retention over time, Geochim. Cosmochim. Acta 360 (2023) 207–230.
[54] P. Wilfert, A. Mandalidis, A.I. Dugulan, K. Goubitz, L. Korving, H. Temmink, G. J. Witkamp, M.C.M. Van Loosdrecht, Vivianite as an important iron phosphate precipitate in sewage treatment plants, Water Res. 104 (2016) 449–460.